Adv Comput Math (2018) 44:327–350
DOI 10.1007/s10444-017-9545-9

High-order positivity-preserving hybrid finite-volume-finite-difference methods for chemotaxis systems

Alina Chertock[1] · Yekaterina Epshteyn[2] · Hengrui Hu[1] · Alexander Kurganov[3,4]

Received: 9 December 2016 / Accepted: 14 June 2017 /
Published online: 21 July 2017

Abstract Chemotaxis refers to mechanisms by which cellular motion occurs in response to an external stimulus, usually a chemical one. Chemotaxis phenomenon plays an important role in bacteria/cell aggregation and pattern formation mechanisms, as well as in tumor growth. A common property of all chemotaxis systems is their ability to model a concentration phenomenon that mathematically results in rapid growth of solutions in small neighborhoods of concentration points/curves. The solutions may blow up or may exhibit a very singular, spiky behavior. There is consequently a need for accurate and computationally efficient numerical methods for

Communicated by: Carlos Garcia-Cervera

✉ Alina Chertock
chertock@math.ncsu.edu

Yekaterina Epshteyn
epshteyn@math.utah.edu

Hengrui Hu
hhu9@ncsu.edu

Alexander Kurganov
kurganov@math.tulane.edu

[1] Department of Mathematics, North Carolina State University, Raleigh, NC 27695, USA

[2] Department of Mathematics, The University of Utah, Salt Lake City, UT 84112, USA

[3] Department of Mathematics, Southern University of Science and Technology of China, Shenzhen, 518055, China

[4] Mathematics Department, Tulane University, New Orleans, LA 70118, USA

the chemotaxis models. In this work, we develop and study novel high-order hybrid finite-volume-finite-difference schemes for the Patlak-Keller-Segel chemotaxis system and related models. We demonstrate high-accuracy, stability and computational efficiency of the proposed schemes in a number of numerical examples.

Keywords Patlak-Keller-Segel chemotaxis system · Advection-diffusion-reaction systems · High-order finite-difference · Finite-volume methods · Positivity-preserving algorithms

Mathematics Subject Classification (2010) 65M06 · 65M08 · 65M12 · 92C17 · 35M10

1 Introduction

We develop and study hybrid finite-volume-finite-difference (FVFD) schemes for the Patlak-Keller-Segel (PKS) chemotaxis system [29–31, 40] and related models. Chemotaxis refers to mechanisms by which cellular motion occurs in response to an external stimulus, usually a chemical one. Chemotaxis phenomenon plays an important role in bacteria/cell aggregation and pattern formation mechanisms, as well as in tumor growth. The PKS model is governed by a system of advection-diffusion-reaction equations, which in the two-dimensional (2-D) case reads as

$$\begin{cases} \rho_t + \nabla\cdot(\chi\rho\nabla c) = \Delta\rho, \\ \alpha c_t = \Delta c - \gamma_c c + \gamma_\rho \rho, \end{cases} \quad (x, y) \in \Omega \subset \mathbb{R}^2, \quad t > 0, \tag{1.1}$$

where $\rho(x, y, t)$ denotes the cell density, $c(x, y, t)$ stands for a chemoattractant concentration, $\chi > 0$ is a chemotactic sensitivity constant, $\gamma_\rho > 0$ and $\gamma_c > 0$ are the reaction coefficients. The parameter α is equal to either 1 or 0, which correspond to the parabolic-parabolic or reduced parabolic-elliptic coupling, respectively.

In the past two decades, chemotaxis systems have been extensively analyzed (see, e.g., [24–27, 42] and references therein). A common property of all chemotaxis systems is their ability to model a concentration phenomenon that mathematically results in rapid growth of solutions in small neighborhoods of concentration points/curves. The solutions may blow up or may exhibit a very singular, spiky behavior. For example, it has been shown that the solution of (1.1) may blow up in finite time, provided the total mass of cells, $\int_\Omega \rho(x, y, 0)dxdy$, is initially above a critical threshold; see, e.g., [8, 26, 27, 41]. This blowup represents a mathematical description of a cell concentration phenomenon that occurs in real biological systems; see, e.g., [1, 5–7, 10, 11, 38, 43].

Capturing blowing up or spiky solutions numerically is a very challenging task, but at the same time development of accurate and efficient numerical methods is crucial for the modeling and analysis of chemotaxis systems. Let us briefly review some of the numerical methods that have been proposed in the literature.

A finite-volume, [21], and finite-element, [37, 44], methods have been proposed for the PKS system with the parabolic-elliptic coupling, that is, the system (1.1) with $\alpha = 0$. A fractional step numerical method for fully time-dependent chemotaxis system from [47, 50] has been proposed in [48]. However, the operator splitting approach may not be applicable for the system (1.1) since its convective part of the chemotaxis system may loose the hyperbolicity. As it has been demonstrated in [9], the latter is a generic situation for the PKS model with parabolic-parabolic ($\alpha = 1$) coupling. Several methods for the parabolic-parabolic PKS system have been recently proposed: a family of high-order discontinuous Galerkin methods has been designed in [14, 15]; an implicit flux-corrected finite-element method has been developed in [45]. These methods achieve high-order of accuracy, but their high memory usage and computational costs are of obvious drawbacks. A simpler and more efficient second-order finite-volume central-upwind scheme has been derived in [9] for the PKS system with $\alpha = 1$ and extended to several more realistic chemotaxis and related models. Finally, in [13] a modified version of the scheme from [9] is extended to PKS system in irregular geometry by employing the idea of the difference potentials.

In this paper, we further improve the scheme from [9] and develop new (high-order) hybrid FVFD schemes: while the density equation in (1.1) is treated using a (high-order) positivity-preserving finite-volume method, a much simpler chemoattractant concentration equation is solved using a simple (high-order) centered-difference scheme. The new schemes are highly accurate, computationally efficient and robust.

The paper is organized as follows. First, in Section 2.1 we design a second-order positivity-preserving hybrid FVFD scheme for the PKS system (1.1). In Section 2.2, we develop a fourth-order positivity-preserving hybrid FVFD method. Finally, in Section 3 we illustrate the performance of the proposed schemes in several numerical experiments. To conduct the experiments in Section 3 we extend the developed methods to the two-species chemotaxis system that was originally proposed and analytically studied in [12, 16–20, 34, 49].

2 Hybrid finite-volume-finite-difference schemes

To derive high-order positivity-preserving numerical schemes for the chemotaxis system (1.1), we first rewrite it in the following equivalent form:

$$\begin{cases} \rho_t + (\chi\rho u - \rho_x)_x + (\chi\rho v - \rho_y)_y = 0, \\ \alpha c_t = \Delta c - \gamma_c c + \gamma_\rho \rho, \end{cases} \qquad u := c_x, \ v := c_y, \tag{2.1}$$

where u and v are the chemotactic velocities.

We consider the system (2.1) in a square domain $\Omega \subset \mathbb{R}^2$, where we introduce a Cartesian mesh consisting of the cells $I_{j,k} := [x_{j-\frac{1}{2}}, x_{j+\frac{1}{2}}] \times [y_{k-\frac{1}{2}}, y_{k+\frac{1}{2}}]$, which, for the sake of simplicity, are assumed to be of the uniform size $\Delta x \Delta y$, that is, $x_{j+\frac{1}{2}} - x_{j-\frac{1}{2}} \equiv \Delta x$ for all j and $y_{k+\frac{1}{2}} - y_{k-\frac{1}{2}} \equiv \Delta y$ for all k. On this mesh, a

general semi-discrete hybrid FVFD scheme for the PKS system (2.1) will have the following form:

$$\begin{cases} \dfrac{d\,\bar{\rho}_{j,k}}{dt} = -\dfrac{\mathcal{F}_{j+\frac{1}{2},k} - \mathcal{F}_{j-\frac{1}{2},k}}{\Delta x} - \dfrac{\mathcal{G}_{j,k+\frac{1}{2}} - \mathcal{G}_{j,k-\frac{1}{2}}}{\Delta y}, \\ \alpha \dfrac{dc_{j,k}}{dt} = \Delta_{j,k} c - \gamma_c c_{j,k} + \gamma_\rho \rho_{j,k}. \end{cases} \tag{2.2}$$

Here, the cell averages of the density, $\bar{\rho}_{j,k}(t) \approx \frac{1}{\Delta x \Delta y} \iint_{I_{j,k}} \rho(x, y, t) dx dy$, and the point values of the chemoattractant concentration, $c_{j,k}(t) \approx c(x_j, y_k, t)$, are the evolved quantities, $\mathcal{F}_{j+\frac{1}{2},k}$ and $\mathcal{G}_{j,k+\frac{1}{2}}$ are the numerical fluxes in the x- and y-directions, respectively, $\Delta_{j,k}$ is a discrete Laplacian, and $\rho_{j,k}(t) \approx \rho(x_j, y_k, t)$ are the approximate point values of the density.

In what follows, we construct the second- (Section 2.1) and fourth-order (Section 2.2) hybrid FVFD schemes. In order to distinguish between the second- and fourth-order numerical fluxes and discrete Laplacians, we will denote them by $\mathcal{F}^{\rm II}_{j+\frac{1}{2},k}$, $\mathcal{G}^{\rm II}_{j,k+\frac{1}{2}}$, $\Delta^{\rm II}_{j,k}$ and $\mathcal{F}^{\rm IV}_{j+\frac{1}{2},k}$, $\mathcal{G}^{\rm IV}_{j,k+\frac{1}{2}}$, $\Delta^{\rm IV}_{j,k}$, respectively.

2.1 Derivation of the second-order scheme

In this section, we present a detailed derivation of the second-order hybrid FVFD scheme of the form (2.2).

We first write the second-order numerical fluxes in (2.2) as follows:

$$\begin{aligned} \mathcal{F}^{\rm II}_{j+\frac{1}{2},k} &= \chi \rho^{\rm II}_{j+\frac{1}{2},k} u^{\rm II}_{j+\frac{1}{2},k} - (\rho_x)^{\rm II}_{j+\frac{1}{2},k}, \\ \mathcal{G}^{\rm II}_{j,k+\frac{1}{2}} &= \chi \rho^{\rm II}_{j,k+\frac{1}{2}} v^{\rm II}_{j,k+\frac{1}{2}} - (\rho_y)^{\rm II}_{j,k+\frac{1}{2}}. \end{aligned} \tag{2.3}$$

The cell density derivatives, $(\rho_x)^{\rm II}_{j+\frac{1}{2},k}$ and $(\rho_y)^{\rm II}_{j,k+\frac{1}{2}}$, and velocities, $u^{\rm II}_{j+\frac{1}{2},k}$ and $v^{\rm II}_{j,k+\frac{1}{2}}$, are approximated using the central differences:

$$\begin{aligned} (\rho_x)^{\rm II}_{j+\frac{1}{2},k} &= \frac{\bar{\rho}_{j+1,k} - \bar{\rho}_{j,k}}{\Delta x}, \qquad (\rho_y)^{\rm II}_{j,k+\frac{1}{2}} = \frac{\bar{\rho}_{j,k+1} - \bar{\rho}_{j,k}}{\Delta y}, \\ u^{\rm II}_{j+\frac{1}{2},k} &= \frac{c_{j+1,k} - c_{j,k}}{\Delta x}, \qquad v^{\rm II}_{j,k+\frac{1}{2}} = \frac{c_{j,k+1} - c_{j,k}}{\Delta y}, \end{aligned} \tag{2.4}$$

while the point values $\rho^{\rm II}_{j+\frac{1}{2},k}$ and $\rho^{\rm II}_{j,k+\frac{1}{2}}$ are computed in an upwind manner:

$$\rho^{\rm II}_{j+\frac{1}{2},k} = \begin{cases} \rho^{\rm E}_{j,k}, & \text{if } u^{\rm II}_{j+\frac{1}{2},k} > 0, \\ \rho^{\rm W}_{j+1,k}, & \text{otherwise}, \end{cases} \qquad \rho^{\rm II}_{j,k+\frac{1}{2}} = \begin{cases} \rho^{\rm N}_{j,k}, & \text{if } v^{\rm II}_{j,k+\frac{1}{2}} > 0, \\ \rho^{\rm S}_{j,k+1}, & \text{otherwise}. \end{cases} \tag{2.5}$$

In (2.5), the one-sided point values at the interfaces, $\rho^{\rm E}_{j,k}$, $\rho^{\rm W}_{j+1,k}$, $\rho^{\rm N}_{j,k}$ and $\rho^{\rm S}_{j,k+1}$, are calculated using a second-order piecewise linear reconstruction

$$\widetilde{\rho}(x, y) = \bar{\rho}_{j,k} + (\rho_x)_{j,k}(x - x_j) + (\rho_y)_{j,k}(y - y_k), \quad (x, y) \in I_{j,k} \tag{2.6}$$

as follows:

$$\begin{aligned}
\rho^{\mathrm{E}}_{j,k} &= \widetilde{\rho}(x_{j+\frac{1}{2}}-0,y_k)=\bar{\rho}_{j,k}+\frac{\Delta x}{2}(\rho_x)_{j,k},\\
\rho^{\mathrm{W}}_{j+1,k} &= \widetilde{\rho}(x_{j+\frac{1}{2}}+0,y_k)=\bar{\rho}_{j+1,k}-\frac{\Delta x}{2}(\rho_x)_{j+1,k},\\
\rho^{\mathrm{N}}_{j,k} &= \widetilde{\rho}(x_j,y_{k+\frac{1}{2}}-0)=\bar{\rho}_{j,k}+\frac{\Delta y}{2}(\rho_y)_{j,k},\\
\rho^{\mathrm{S}}_{j,k+1} &= \widetilde{\rho}(x_j,y_{k+\frac{1}{2}}+0)=\bar{\rho}_{j,k+1}-\frac{\Delta y}{2}(\rho_y)_{j,k+1}.
\end{aligned} \tag{2.7}$$

In order to ensure that the point values in (2.7) are both second-order and nonnegative, the slopes in (2.6) are calculated adaptively using

$$(\rho_x)_{j,k}=\begin{cases}
\dfrac{\bar{\rho}_{j+1,k}-\bar{\rho}_{j-1,k}}{2\Delta x},\\
\text{if } \bar{\rho}_{j,k}\pm\dfrac{\Delta x}{2}\cdot\dfrac{\bar{\rho}_{j+1,k}-\bar{\rho}_{j-1,k}}{2\Delta x}=\bar{\rho}_{j,k}\pm\dfrac{\bar{\rho}_{j+1,k}-\bar{\rho}_{j-1,k}}{4}\geq 0,\\
\text{minmod}\Big(2\dfrac{\bar{\rho}_{j+1,k}-\bar{\rho}_{j,k}}{\Delta x},\ \dfrac{\bar{\rho}_{j+1,k}-\bar{\rho}_{j-1,k}}{2\Delta x},\ 2\dfrac{\bar{\rho}_{j,k}-\bar{\rho}_{j-1,k}}{\Delta x}\Big),\\
\text{otherwise},
\end{cases}$$

$$(\rho_y)_{j,k}=\begin{cases}
\dfrac{\bar{\rho}_{j,k+1}-\bar{\rho}_{j,k-1}}{2\Delta y},\\
\text{if } \bar{\rho}_{j,k}\pm\dfrac{\Delta y}{2}\cdot\dfrac{\bar{\rho}_{j,k+1}-\bar{\rho}_{j,k-1}}{2\Delta y}=\bar{\rho}_{j,k}\pm\dfrac{\bar{\rho}_{j,k+1}-\bar{\rho}_{j,k-1}}{4}\geq 0,\\
\text{minmod}\Big(2\dfrac{\bar{\rho}_{j,k+1}-\bar{\rho}_{j,k}}{\Delta y},\ \dfrac{\bar{\rho}_{j,k+1}-\bar{\rho}_{j,k-1}}{2\Delta y},\ 2\dfrac{\bar{\rho}_{j,k}-\bar{\rho}_{j,k-1}}{\Delta y}\Big),\\
\text{otherwise}.
\end{cases} \tag{2.8}$$

Here,

$$\text{minmod}(z_1,z_2,\ldots):=\begin{cases}
\min(z_1,z_2,\ldots), & \text{if } z_i>0\ \forall i,\\
\max(z_1,z_2,\ldots), & \text{if } z_i<0\ \forall i,\\
0, & \text{otherwise},
\end{cases}$$

and the positivity of reconstructed point values is ensured by the positivity-preserving generalized minmod limiter, [35, 36, 39, 46], under the assumption that the cell averages of ρ are nonnegative.

Remark 1 We note that the minmod limiter used in (2.8) can be replaced with another (positivity-preserving) nonlinear limiter; see, e.g., [35, 36, 39, 46].

Next, we use the standard five-point stencil to obtain a second-order approximate Laplace operator in (2.2):

$$\Delta^{\mathrm{II}}_{j,k}c=\frac{c_{j+1,k}-2c_{j,k}+c_{j-1,k}}{(\Delta x)^2}+\frac{c_{j,k+1}-2c_{j,k}+c_{j,k-1}}{(\Delta y)^2}. \tag{2.9}$$

This completes the derivation and the resulting second-order semi-discrete hybrid FVFD scheme is

$$\begin{cases} \dfrac{d\,\bar{\rho}_{j,k}}{dt} = -\dfrac{\mathcal{F}^{\rm II}_{j+\frac{1}{2},k} - \mathcal{F}^{\rm II}_{j-\frac{1}{2},k}}{\Delta x} - \dfrac{\mathcal{G}^{\rm II}_{j,k+\frac{1}{2}} - \mathcal{G}^{\rm II}_{j,k-\frac{1}{2}}}{\Delta y}, \\ \alpha \dfrac{dc_{j,k}}{dt} = \Delta^{\rm II}_{j,k} c - \gamma_c c_{j,k} + \gamma_\rho\, \bar{\rho}_{j,k}. \end{cases} \tag{2.10}$$

We now consider the cases $\alpha = 1$ and $\alpha = 0$ separately.

Parabolic-Parabolic Case ($\alpha = 1$) In this case, the obtained scheme (2.10) is a system of time-dependent ODEs, which has to be numerically integrated using a stable and accurate ODE solver. In our numerical experiments, we use strong stability preserving Runge-Kutta methods (SSP RK); see, e.g., [22, 23]. The SSP property is essential for the resulting fully discrete scheme to preserve positivity of both $\{\bar{\rho}_{j,k}\}$ and $\{c_{j,k}\}$ as stated in the following theorem. We prove this result for the first-order forward Euler discretization, but it is also valid for the SSP methods, whose time steps are convex combinations of several forward Euler steps.

Theorem 1 *Assume that the system of ODEs (2.10) with $\alpha = 1$, (2.3)–(2.9) is integrated using the forward Euler method:*

$$\begin{aligned} \bar{\rho}_{j,k}(t+\Delta t) &= \bar{\rho}_{j,k}(t) - \lambda\big(\mathcal{F}^{\rm II}_{j+\frac{1}{2},k}(t) - \mathcal{F}^{\rm II}_{j-\frac{1}{2},k}(t)\big) \\ &\quad -\mu\big(\mathcal{G}^{\rm II}_{j,k+\frac{1}{2}}(t) - \mathcal{G}^{\rm II}_{j,k-\frac{1}{2}}(t)\big), \qquad (2.11) \\ c_{j,k}(t+\Delta t) &= (1-\Delta t\gamma_c)c_{j,k}(t) + \Delta t \Delta^{II}_{j,k} c(t) + \Delta t \gamma_\rho\, \bar{\rho}_{j,k}(t), \qquad (2.12) \end{aligned}$$

where $\lambda := \Delta t/\Delta x$ and $\mu := \Delta t/\Delta y$. Then, the evolved cell densities, $\bar{\rho}_{j,k}(t+\Delta t)$, and chemoattractant concentrations, $c_{j,k}(t+\Delta t)$, will be nonnegative for all j,k provided $\bar{\rho}_{j,k}(t)$ and $c_{j,k}(t)$ are nonnegative for all j,k and the following CFL-like condition is satisfied:

$$\Delta t \le \min\left\{\frac{\Delta x}{8a}, \frac{\Delta y}{8b}, \frac{\Delta x \Delta y}{4K}, \frac{1}{\max\{K_1, \varepsilon\}}\right\}, \tag{2.13}$$

where

$$\begin{aligned} &a := \chi \max_{j,k} |u^{II}_{j+\frac{1}{2},k}|, \quad b := \chi \max_{j,k} |v^{II}_{j,k+\frac{1}{2}}|, \\ &K := \frac{\Delta x}{\Delta y} + \frac{\Delta y}{\Delta x}, \quad K_1 := \max_{j,k}\left(\gamma_c + \frac{2K}{\Delta x \Delta y} - \frac{\gamma_\rho \bar{\rho}_{j,k}}{c_{j,k}}\right). \end{aligned} \tag{2.14}$$

Proof We follow the lines of the positivity proof in [9]. We begin with the cell density equation (2.11) and note that the positivity-preserving property of the interpolant (2.6) will guarantee that the reconstructed point values $\rho^{\rm E}_{j,k}, \rho^{\rm W}_{j,k}, \rho^{\rm N}_{j,k}$ and $\rho^{\rm S}_{j,k}$ will be nonnegative provided $\bar{\rho}_{j,k}(t) \ge 0,\ \forall j,k$. We then use (2.3)–(2.5) and the conser-

vation property for the cell densities, $\bar{\rho}_{j,k} = \frac{1}{8}(\rho^{\mathrm{E}}_{j,k} + \rho^{\mathrm{W}}_{j,k} + \rho^{\mathrm{S}}_{j,k} + \rho^{\mathrm{N}}_{j,k}) + \frac{1}{2}\,\bar{\rho}_{j,k}$, to regroup the terms in (2.11) as follows:

$$
\begin{aligned}
\bar{\rho}_{j,k}(t+\Delta t) = &\left[\frac{1}{8} - \frac{\lambda\chi}{2}\left(|u^{\mathrm{II}}_{j-\frac{1}{2},k}| - u^{\mathrm{II}}_{j-\frac{1}{2},k}\right)\right]\rho^{\mathrm{W}}_{j,k} \\
&+\left[\frac{1}{8} - \frac{\lambda\chi}{2}\left(|u^{\mathrm{II}}_{j+\frac{1}{2},k}| + u^{\mathrm{II}}_{j+\frac{1}{2},k}\right)\right]\rho^{\mathrm{E}}_{j,k} + \frac{\lambda\chi}{2}\left(|u^{\mathrm{II}}_{j+\frac{1}{2},k}| - u^{\mathrm{II}}_{j+\frac{1}{2},k}\right)\rho^{\mathrm{W}}_{j+1,k} \\
&+\frac{\lambda\chi}{2}\left(|u^{\mathrm{II}}_{j-\frac{1}{2},k}| + u^{\mathrm{II}}_{j-\frac{1}{2},k}\right)\rho^{\mathrm{E}}_{j-1,k} + \left[\frac{1}{8} - \frac{\mu\chi}{2}\left(|v^{\mathrm{II}}_{j,k-\frac{1}{2}}| - v^{\mathrm{II}}_{j,k-\frac{1}{2}}\right)\right]\rho^{\mathrm{S}}_{j,k} \\
&+\left[\frac{1}{8} - \frac{\mu\chi}{2}\left(|v^{\mathrm{II}}_{j,k+\frac{1}{2}}| + v^{\mathrm{II}}_{j,k+\frac{1}{2}}\right)\right]\rho^{\mathrm{N}}_{j,k} + \frac{\mu\chi}{2}\left(|v^{\mathrm{II}}_{j,k+\frac{1}{2}}| - v^{\mathrm{II}}_{j,k+\frac{1}{2}}\right)\rho^{\mathrm{S}}_{j,k+1} \\
&+\frac{\mu\chi}{2}\left(|v^{\mathrm{II}}_{j,k-\frac{1}{2}}| + v^{\mathrm{II}}_{j,k-\frac{1}{2}}\right)\rho^{\mathrm{N}}_{j,k-1} + \bar{\rho}_{j,k}(t)\left[\frac{1}{2} - \frac{2K\Delta t}{\Delta x \Delta y}\right] \\
&+\Delta t\left[\frac{\bar{\rho}_{j+1,k}(t) + \bar{\rho}_{j-1,k}(t)}{(\Delta x)^2} + \frac{\bar{\rho}_{j,k+1}(t) + \bar{\rho}_{j,k-1}(t)}{(\Delta y)^2}\right].
\end{aligned}
$$

As one can see, $\bar{\rho}_{j,k}(t + \Delta t)$ is a linear combination of the cell averages $\bar{\rho}_{j,k}(t)$, $\bar{\rho}_{j\pm1,k}(t)$, $\bar{\rho}_{j,k\pm1}(t)$ and the reconstructed point values $\rho^{\mathrm{W}}_{j,k}$, $\rho^{\mathrm{E}}_{j,k}$, $\rho^{\mathrm{W}}_{j+1,k}$, $\rho^{\mathrm{E}}_{j-1,k}$, $\rho^{\mathrm{S}}_{j,k}$, $\rho^{\mathrm{N}}_{j,k}$, $\rho^{\mathrm{S}}_{j,k+1}$, $\rho^{\mathrm{N}}_{j,k-1}$, which are nonnegative. The coefficients of this linear combination are also nonnegative under the CFL-like condition (2.13), which guarantees that $\bar{\rho}_{j,k}(t + \Delta t) \geq 0$ for all j, k.

Finally, the CFL-like condition (2.13) ensures that all of the terms on the right-hand side (RHS) of (2.12) are nonnegative and thus $c_{j,k}(t + \Delta t) \geq 0$ for all j, k, which completes the proof of the theorem. □

Parabolic-Elliptic Case ($\alpha = 0$) In this case, the scheme (2.10) is a system of differential-algebraic equations (DAEs). The second equation in (2.10) now reduces to a system of linear algebraic equations for $c_{j,k}$, which is to be solved by an accurate and efficient linear algebra solver. It should be observed that the matrix of this linear system is diagonally dominant, which would guarantee the positivity of c, while the positivity of ρ is enforced the same way as in the parabolic-parabolic case, but with a different CFL-like condition as summarized in the following theorem.

Theorem 2 *Assume that the first equation of the system of DAEs (2.10) with $\alpha = 0$, (2.3)–(2.9) is integrated using the forward Euler method resulting in equation (2.11), while the system of linear algebraic equations for $c_{j,k}$ is solved exactly. Then, the evolved cell densities, $\bar{\rho}_{j,k}(t+\Delta t)$, and chemoattractant concentrations, $c_{j,k}(t+\Delta t)$, will be nonnegative for all j, k provided $\bar{\rho}_{j,k}(t)$ and $c_{j,k}(t)$ are nonnegative for all j, k and the following CFL-like condition is satisfied:*

$$
\Delta t \leq \min\left\{\frac{\Delta x}{8a}, \frac{\Delta y}{8b}, \frac{\Delta x \Delta y}{4K}\right\},
$$

where a, b and K are given by (2.14).

2.2 Derivation of the fourth-order scheme

In this section, we present a detailed derivation of the fourth-order hybrid FVFD scheme of the form (2.2).

We first write the fourth-order numerical fluxes as follows:

$$\mathcal{F}^{\rm IV}_{j+\frac{1}{2},k}=\chi(\rho u)^{\rm IV}_{j+\frac{1}{2},k}-(\rho_x)^{\rm IV}_{j+\frac{1}{2},k},\quad \mathcal{G}^{\rm IV}_{j,k+\frac{1}{2}}=\chi(\rho v)^{\rm IV}_{j,k+\frac{1}{2}}-(\rho_y)^{\rm IV}_{j,k+\frac{1}{2}}. \tag{2.15}$$

As in the case of the second-order scheme, the cell density derivatives are approximated using the central differences:

$$\begin{aligned}(\rho_x)^{\rm IV}_{j+\frac{1}{2},k}&=\frac{\bar\rho_{j-1,k}-15\,\bar\rho_{j,k}+15\,\bar\rho_{j+1,k}-\bar\rho_{j+2,k}}{12\Delta x},\\ (\rho_y)^{\rm IV}_{j,k+\frac{1}{2}}&=\frac{\bar\rho_{j,k-1}-15\,\bar\rho_{j,k}+15\,\bar\rho_{j,k+1}-\bar\rho_{j,k+2}}{12\Delta y}\end{aligned} \tag{2.16}$$

while the chemotactic flux terms are computed in an upwind manner:

$$\begin{aligned}(\rho u)^{\rm IV}_{j+\frac{1}{2},k}&=\begin{cases}\rho^{\rm NE}_{j,k}u_{j+\frac{1}{2},k+\frac{1}{2}}+4\rho^{\rm E}_{j,k}u_{j+\frac{1}{2},k}+\rho^{\rm SE}_{j,k}u_{j+\frac{1}{2},k-\frac{1}{2}},\\ \quad\text{if } u_{j+\frac{1}{2},k}>0,\\ \rho^{\rm NW}_{j+1,k}u_{j+\frac{1}{2},k+\frac{1}{2}}+4\rho^{\rm W}_{j+1,k}u_{j+\frac{1}{2},k}+\rho^{\rm SW}_{j+1,k}u_{j+\frac{1}{2},k-\frac{1}{2}},\\ \quad\text{otherwise},\end{cases}\\ (\rho v)^{\rm IV}_{j,k+\frac{1}{2}}&=\begin{cases}\rho^{\rm NW}_{j,k}v_{j-\frac{1}{2},k+\frac{1}{2}}+4\rho^{\rm N}_{j,k}v_{j,k+\frac{1}{2}}+\rho^{\rm NE}_{j,k}v_{j+\frac{1}{2},k+\frac{1}{2}},\\ \quad\text{if } v_{j,k+\frac{1}{2}}>0,\\ \rho^{\rm SW}_{j,k+1}v_{j-\frac{1}{2},k+\frac{1}{2}}+4\rho^{\rm S}_{j,k+1}v_{j,k+\frac{1}{2}}+\rho^{\rm SE}_{j,k+1}v_{j+\frac{1}{2},k+\frac{1}{2}},\\ \quad\text{otherwise}.\end{cases}\end{aligned} \tag{2.17}$$

The velocities u and v in (2.17) are obtained using the fourth-order central differences:

$$\begin{aligned}u_{j+\frac{1}{2},k}&=\frac{c_{j-1,k}-27c_{j,k}+27c_{j+1,k}-c_{j+2,k}}{24\Delta x},\\ v_{j,k+\frac{1}{2}}&=\frac{c_{j,k-1}-27c_{j,k}+27c_{j,k+1}-c_{j,k+2}}{24\Delta y},\end{aligned} \tag{2.18}$$

and

$$\begin{aligned}u_{j+\frac{1}{2},k+\frac{1}{2}}&=\frac{1}{48\Delta x}\Big[30(c_{j+1,k+1}-c_{j,k+1}+c_{j+1,k}-c_{j,k})\\ &\quad-3(c_{j+1,k+2}-c_{j,k+2}+c_{j+1,k-1}-c_{j,k-1})\\ &\quad-(c_{j+2,k+1}-c_{j-1,k+1}+c_{j+2,k}-c_{j-1,k})\Big],\\ v_{j+\frac{1}{2},k+\frac{1}{2}}&=\frac{1}{48\Delta y}\Big[30(c_{j+1,k+1}-c_{j+1,k}+c_{j,k+1}-c_{j,k})\\ &\quad-3(c_{j+2,k+1}-c_{j+2,k}+c_{j-1,k+1}\\ &\quad-c_{j-1,k})-(c_{j+1,k+2}-c_{j+1,k-1}+c_{j,k+2}-c_{j,k-1})\Big].\end{aligned} \tag{2.19}$$

The discrete point values of the cell density along the interfaces, $\rho^{\mathrm{E}}_{j,k}$, $\rho^{\mathrm{W}}_{j,k}$, $\rho^{\mathrm{N}}_{j,k}$, $\rho^{\mathrm{S}}_{j,k}$, $\rho^{\mathrm{NE}}_{j,k}$, $\rho^{\mathrm{NW}}_{j,k}$, $\rho^{\mathrm{SE}}_{j,k}$ and $\rho^{\mathrm{SW}}_{j,k}$, are calculated using a fourth-order piecewise polynomial reconstruction

$$\widetilde{\rho}(x,y)=\sum_{j,k}\mathcal{P}_{j,k}(x,y)\mathbb{1}_{j,k}(x,y) \tag{2.20}$$

as follows:

$$\begin{aligned}
&\rho^{\mathrm{E}}_{j,k}=\widetilde{\rho}(x_{j+\frac{1}{2}}-0,y_k),\ \rho^{\mathrm{W}}_{j,k}=\widetilde{\rho}(x_{j-\frac{1}{2}}+0,y_k),\\
&\rho^{\mathrm{N}}_{j,k}=\widetilde{\rho}(x_j,y_{k+\frac{1}{2}}-0),\ \rho^{\mathrm{S}}_{j,k}=\widetilde{\rho}(x_j,y_{k-\frac{1}{2}}+0),\\
&\rho^{\mathrm{NE}}_{j,k}=\widetilde{\rho}(x_{j+\frac{1}{2}}-0,y_{k+\frac{1}{2}}-0),\ \rho^{\mathrm{NW}}_{j,k}=\widetilde{\rho}(x_{j-\frac{1}{2}}+0,y_{k+\frac{1}{2}}-0),\\
&\rho^{\mathrm{SE}}_{j,k}=\widetilde{\rho}(x_{j+\frac{1}{2}}-0,y_{k-\frac{1}{2}}+0),\ \rho^{\mathrm{SW}}_{j,k}=\widetilde{\rho}(x_{j-\frac{1}{2}}+0,y_{k-\frac{1}{2}}+0).
\end{aligned} \tag{2.21}$$

In (2.20), $\mathbb{1}_{j,k}(x,y)$ is the characteristic function of cell $I_{j,k}$, and the polynomials $\mathcal{P}_{j,k}(x,y)$ are

$$\begin{aligned}
\mathcal{P}_{j,k}(x,y)=\ &\rho_{j,k}+(\rho_x)_{j,k}(x-x_j)+(\rho_y)_{j,k}(y-y_k)\\
&+\frac{1}{2}(\rho_{xx})_{j,k}(x-x_j)^2+(\rho_{xy})_{j,k}(x-x_j)(y-y_k)\\
&+\frac{1}{2}(\rho_{yy})_{j,k}(y-y_k)^2\\
&+\frac{1}{6}(\rho_{xxx})_{j,k}(x-x_j)^3+\frac{1}{2}(\rho_{xxy})_{j,k}(x-x_j)^2(y-y_k)\\
&+\frac{1}{2}(\rho_{xyy})_{j,k}(x-x_j)(y-y_k)^2+\frac{1}{6}(\rho_{yyy})_{j,k}(y-y_k)^3\\
&+\frac{1}{24}(\rho_{xxxx})_{j,k}(x-x_j)^4+\frac{1}{4}(\rho_{xxyy})_{j,k}(x-x_j)^2(y-y_k)^2\\
&+\frac{1}{24}(\rho_{yyyy})_{j,k}(y-y_k)^4
\end{aligned} \tag{2.22}$$

with the coefficients calculated from the following 13 conservation requirements (see [32, Appendix B] for details including the precise expressions for the reconstructed point values of ρ in terms of its cell averages):

$$\frac{1}{\Delta x\Delta y}\iint\limits_{I_{j+m,k+\ell}}\mathcal{P}_{j,k}(x,y)\,dxdy=\bar{\rho}_{j+m,k+\ell},\quad \{m,\ell\in\mathbb{Z}:\ |m|+|\ell|\le 2\}. \tag{2.23}$$

Next, we use the nine-point stencil to obtain a fourth-order approximate Laplace operator,

$$\begin{aligned}
\Delta^{\mathrm{IV}}_{j,k}c=\ &\frac{-c_{j-2,k}+16c_{j-1,k}-30c_{j,k}+16c_{j+1,k}-c_{j+2,k}}{12(\Delta x)^2}\\
&+\frac{-c_{j,k-2}+16c_{j,k-1}-30c_{j,k}+16c_{j,k+1}-c_{j,k+2}}{12(\Delta y)^2},
\end{aligned}$$

which can be rewritten in terms of diffusion fluxes as

$$\Delta^{\rm IV}_{j,k}c=-\frac{\mathcal{H}^{\rm IV}_{j+\frac{1}{2},k}-\mathcal{H}^{\rm IV}_{j-\frac{1}{2},k}}{\Delta x}-\frac{\mathcal{L}^{\rm IV}_{j,k+\frac{1}{2}}-\mathcal{L}^{\rm IV}_{j,k-\frac{1}{2}}}{\Delta y} \tag{2.24}$$

with

$$\begin{aligned}\mathcal{H}^{\rm IV}_{j+\frac{1}{2},k}&=\frac{-c_{j-1,k}+15c_{j,k}-15c_{j+1,k}+c_{j+2,k}}{12\Delta x},\\ \mathcal{L}^{\rm IV}_{j,k+\frac{1}{2}}&=\frac{-c_{j,k-1}+15c_{j,k}-15c_{j,k+1}+c_{j,k+2}}{12\Delta y}.\end{aligned} \tag{2.25}$$

The obtained fourth-order semi-discrete hybrid FVFD scheme is

$$\begin{cases}\dfrac{d\,\bar\rho_{j,k}}{dt}=-\dfrac{\mathcal{F}^{\rm IV}_{j+\frac{1}{2},k}-\mathcal{F}^{\rm IV}_{j-\frac{1}{2},k}}{\Delta x}-\dfrac{\mathcal{G}^{\rm IV}_{j,k+\frac{1}{2}}-\mathcal{G}^{\rm IV}_{j,k-\frac{1}{2}}}{\Delta y},\\ \alpha\dfrac{dc_{j,k}}{dt}=-\dfrac{\mathcal{H}^{\rm IV}_{j+\frac{1}{2},k}-\mathcal{H}^{\rm IV}_{j-\frac{1}{2},k}}{\Delta x}-\dfrac{\mathcal{L}^{\rm IV}_{j,k+\frac{1}{2}}-\mathcal{L}^{\rm IV}_{j,k-\frac{1}{2}}}{\Delta y}-\gamma_c c_{j,k}+\gamma_\rho\rho_{j,k},\end{cases} \tag{2.26}$$

where $\rho_{j,k}$ is a point value of ρ at the center of cell $I_{j,k}$ given by

$$\begin{aligned}\rho_{j,k}=\frac{1}{5760}\Big[&27\big(\bar\rho_{j-2,k}+\bar\rho_{j,k-2}+\bar\rho_{j,k+2}+\bar\rho_{j+2,k}\big)\\ &+10\big(\bar\rho_{j-1,k-1}+\bar\rho_{j-1,k+1}+\bar\rho_{j+1,k-1}+\bar\rho_{j+1,k+1}\big)\\ &-368\big(\bar\rho_{j-1,k}+\bar\rho_{j,k-1}+\bar\rho_{j,k+1}+\bar\rho_{j+1,k}\big)+7084\,\bar\rho_{j,k}\Big].\end{aligned} \tag{2.27}$$

As in the case of the second-order scheme, we consider the cases $\alpha=1$ and $\alpha=0$ separately.

Parabolic-Parabolic Case ($\alpha=1$) In this case, the obtained scheme (2.26) is a system of time-dependent ODEs, which, as before, has to be numerically integrated. Unfortunately, even if one uses an SSP ODE solver, positivity of ρ and c cannot be guaranteed. We therefore modify the numerical fluxes following the approach proposed in [4] in the context of shallow water models.

For simplicity of presentation, we consider the forward Euler time discretization of (2.26):

$$\begin{aligned}\bar\rho_{j,k}(t+\Delta t)=\bar\rho_{j,k}(t)&-\lambda\big(\mathcal{F}^{\rm IV}_{j+\frac{1}{2},k}(t)-\mathcal{F}^{\rm IV}_{j-\frac{1}{2},k}(t)\big)\\ &-\mu\big(\mathcal{G}^{\rm IV}_{j,k+\frac{1}{2}}(t)-\mathcal{G}^{\rm IV}_{j,k-\frac{1}{2}}(t)\big),\\ c_{j,k}(t+\Delta t)=(1-\Delta t\gamma_c)c_{j,k}(t)&+\Delta t\gamma_\rho\rho_{j,k}(t)\\ &-\lambda\big(\mathcal{H}^{\rm IV}_{j+\frac{1}{2},k}(t)-\mathcal{H}^{\rm IV}_{j-\frac{1}{2},k}(t)\big)-\mu\big(\mathcal{L}^{\rm IV}_{j,k+\frac{1}{2}}(t)-\mathcal{L}^{\rm IV}_{j,k-\frac{1}{2}}(t)\big),\end{aligned} \tag{2.28}$$

where Δt is selected according to the CFL-like condition similar to (2.13). In order to design a positivity-preserving algorithm, we first introduce "draining" time steps:

$$\begin{aligned}\Delta t^{\rho}_{j,k} &:= \frac{\Delta x\Delta y\,\bar{\rho}_{j,k}(t)}{f^{\rho}_{j,k}\Delta y + g^{\rho}_{j,k}\Delta x},\\ \Delta t^{c}_{j,k} &:= \frac{\Delta x\Delta y[(1-\Delta t\gamma_c)c_{j,k}(t) + \Delta t\gamma_\rho\rho_{j,k}(t)]}{f^{c}_{j,k}\Delta y + g^{c}_{j,k}\Delta x},\end{aligned} \tag{2.29}$$

where

$$\begin{aligned}f^{\rho}_{j,k} &:= \max(\mathcal{F}^{\mathrm{IV}}_{j+\frac{1}{2},k},0) + \max(-\mathcal{F}^{\mathrm{IV}}_{j-\frac{1}{2},k},0),\\ g^{\rho}_{j,k} &:= \max(\mathcal{G}^{\mathrm{IV}}_{j,k+\frac{1}{2}},0) + \max(-\mathcal{G}^{\mathrm{IV}}_{j,k-\frac{1}{2}},0),\\ f^{c}_{j,k} &:= \max(\mathcal{H}^{\mathrm{IV}}_{j+\frac{1}{2},k},0) + \max(-\mathcal{H}^{\mathrm{IV}}_{j-\frac{1}{2},k},0),\\ g^{c}_{j,k} &:= \max(\mathcal{L}^{\mathrm{IV}}_{j,k+\frac{1}{2}},0) + \max(-\mathcal{L}^{\mathrm{IV}}_{j,k-\frac{1}{2}},0).\end{aligned} \tag{2.30}$$

We note that one can easily show that under the following time step restriction:

$$\Delta t \le \min_{j,k}\left\{\min\left(\Delta t^{\rho}_{j,k},\Delta t^{c}_{j,k}\right)\right\}, \tag{2.31}$$

the fully discrete scheme (2.28) is positivity preserving. However, the time step bound (2.31) is too severe and impractical since it may lead to appearance of very small and decreasing time steps, which will not only make the scheme inefficient, but may simply not allow the code to run until the final computational time.

We therefore follow the idea in [4] and define the following quantities:

$$\begin{aligned}\Delta t^{\rho}_{j+\frac{1}{2},k} &:= \min(\Delta t,\Delta t^{\rho}_{m,k}), \quad m = j+\frac{1}{2}-\frac{\mathrm{sgn}(\mathcal{F}^{\mathrm{IV}}_{j+\frac{1}{2},k})}{2},\\ \Delta t^{\rho}_{j,k+\frac{1}{2}} &:= \min(\Delta t,\Delta t^{\rho}_{j,\ell}), \quad \ell = k+\frac{1}{2}-\frac{\mathrm{sgn}(\mathcal{G}^{\mathrm{IV}}_{j,k+\frac{1}{2}})}{2},\\ \Delta t^{c}_{j+\frac{1}{2},k} &:= \min(\Delta t,\Delta t^{c}_{p,k}), \quad p = j+\frac{1}{2}-\frac{\mathrm{sgn}(\mathcal{H}^{\mathrm{IV}}_{j+\frac{1}{2},k})}{2},\\ \Delta t^{c}_{j,k+\frac{1}{2}} &:= \min(\Delta t,\Delta t^{c}_{j,q}), \quad q = k+\frac{1}{2}-\frac{\mathrm{sgn}(\mathcal{L}^{\mathrm{IV}}_{j,k+\frac{1}{2}})}{2},\end{aligned} \tag{2.32}$$

and use them to replace the numerical fluxes in (2.28) with

$$\begin{aligned}\widehat{\mathcal{F}}^{\mathrm{IV}}_{j+\frac{1}{2},k} &= \frac{\Delta t^{\rho}_{j+\frac{1}{2},k}}{\Delta t}\mathcal{F}^{\mathrm{IV}}_{j+\frac{1}{2},k}, \quad \widehat{\mathcal{G}}^{\mathrm{IV}}_{j,k+\frac{1}{2}} = \frac{\Delta t^{\rho}_{j,k+\frac{1}{2}}}{\Delta t}\mathcal{G}^{\mathrm{IV}}_{j,k+\frac{1}{2}}\\ \widehat{\mathcal{H}}^{\mathrm{IV}}_{j+\frac{1}{2},k} &= \frac{\Delta t^{c}_{j+\frac{1}{2},k}}{\Delta t}\mathcal{H}^{\mathrm{IV}}_{j+\frac{1}{2},k}, \quad \widehat{\mathcal{L}}^{\mathrm{IV}}_{j,k+\frac{1}{2}} = \frac{\Delta t^{c}_{j,k+\frac{1}{2}}}{\Delta t}\mathcal{L}^{\mathrm{IV}}_{j,k+\frac{1}{2}}.\end{aligned} \tag{2.33}$$

The modified version of the fully discrete scheme (2.28) then reads as

$$\bar{\rho}_{j,k}(t+\Delta t)=\bar{\rho}_{j,k}(t)-\lambda\big(\widehat{\mathcal{F}}^{\rm IV}_{j+\frac12,k}(t)-\widehat{\mathcal{F}}^{\rm IV}_{j-\frac12,k}(t)\big)$$
$$-\mu\big(\widehat{\mathcal{G}}^{\rm IV}_{j,k+\frac12}(t)-\widehat{\mathcal{G}}^{\rm IV}_{j,k-\frac12}(t)\big), \tag{2.34}$$

$$c_{j,k}(t+\Delta t)=(1-\Delta t\gamma_c)c_{j,k}(t)+\Delta t\gamma_\rho\rho_{j,k}(t)$$
$$-\lambda\big(\widehat{\mathcal{H}}^{\rm IV}_{j+\frac12,k}(t)-\widehat{\mathcal{H}}^{\rm IV}_{j-\frac12,k}(t)\big)-\mu\big(\widehat{\mathcal{L}}^{\rm IV}_{j,k+\frac12}(t)-\widehat{\mathcal{L}}^{\rm IV}_{j,k-\frac12}(t)\big). \tag{2.35}$$

We now prove its positivity-preserving property.

Theorem 3 *The cell densities $\bar{\rho}_{j,k}(t+\Delta t)$ and chemoattractant concentrations $c_{j,k}(t+\Delta t)$, computed by the fully discrete scheme (2.34), (2.35), (2.29), (2.30), (2.32), (2.33), (2.15)–(2.25) will be nonnegative provided $\bar{\rho}_{j,k}(t)$ and $c_{j,k}(t)$ are nonnegative for all j,k.*

Proof In order to prove positivity of ρ, one needs to consider different cases depending on the sign of the fluxes $\mathcal{F}^{\rm IV}_{j+\frac12,k}$ and $\mathcal{G}^{\rm IV}_{j,k+\frac12}$ given by (2.15). We will only consider one of these cases, namely, assuming that

$$\mathcal{F}^{\rm IV}_{j+\frac12,k}>0,\quad \mathcal{F}^{\rm IV}_{j-\frac12,k}>0\quad\text{and}\quad \mathcal{G}^{\rm IV}_{j,k+\frac12}<0,\quad \mathcal{G}^{\rm IV}_{j,k-\frac12}<0. \tag{2.36}$$

in the cell $I_{j,k}$. All of the other cases can be analyzed in a similar way.

First, we use the definitions in (2.30) to obtain

$$f^{\rho}_{j,k}=\mathcal{F}^{\rm IV}_{j+\frac12,k},\quad g^{\rho}_{j,k}=-\mathcal{G}^{\rm IV}_{j,k-\frac12}, \tag{2.37}$$

and then substituting (2.37) into (2.29) results in

$$\Delta t^{\rho}_{j,k}=\frac{\Delta x\Delta y\,\bar{\rho}_{j,k}(t)}{\mathcal{F}^{\rm IV}_{j+\frac12,k}\Delta y-\mathcal{G}^{\rm IV}_{j,k-\frac12}\Delta x}>0. \tag{2.38}$$

It also follows from (2.36) and (2.32) that

$$\begin{aligned}&\Delta t^{\rho}_{j+\frac12,k}=\min(\Delta t,\Delta t^{\rho}_{j,k}),\qquad &&\Delta t^{\rho}_{j-\frac12,k}=\min(\Delta t,\Delta t^{\rho}_{j-1,k}),\\ &\Delta t^{\rho}_{j,k+\frac12}=\min(\Delta t,\Delta t^{\rho}_{j,k+1}),\qquad &&\Delta t^{\rho}_{j,k-\frac12}=\min(\Delta t,\Delta t^{\rho}_{j,k}).\end{aligned} \tag{2.39}$$

We now rewrite the cell density equation (2.34) as

$$\bar{\rho}_{j,k}(t+\Delta t)=\bar{\rho}_{j,k}(t)+\frac{\Delta t^{\rho}_{j-\frac12,k}}{\Delta x}\mathcal{F}^{\rm IV}_{j-\frac12,k}-\frac{\Delta t^{\rho}_{j,k+\frac12}}{\Delta y}\mathcal{G}^{\rm IV}_{j,k+\frac12}$$
$$+\frac{\Delta t^{\rho}_{j,k-\frac12}}{\Delta y}\mathcal{G}^{\rm IV}_{j,k-\frac12}-\frac{\Delta t^{\rho}_{j+\frac12,k}}{\Delta x}\mathcal{F}^{\rm IV}_{j+\frac12,k}, \tag{2.40}$$

and show that the RHS of (2.40) is positive. To this end, we first note that (2.36) implies

$$\frac{\Delta t^{\rho}_{j-\frac12,k}}{\Delta x}\mathcal{F}^{\rm IV}_{j-\frac12,k}-\frac{\Delta t^{\rho}_{j,k+\frac12}}{\Delta y}\mathcal{G}^{\rm IV}_{j,k+\frac12}>0. \tag{2.41}$$

We then note that $\Delta t^{\rho}_{j+\frac{1}{2},k} = \Delta t^{\rho}_{j,k-\frac{1}{2}} \le \Delta t^{\rho}_{j,k}$, and therefore using (2.38), (2.40) and (2.41), we conclude with

$$\begin{aligned}\bar{\rho}_{j,k}(t+\Delta t) &> \bar{\rho}_{j,k}(t) + \frac{\Delta t^{\rho}_{j,k-\frac{1}{2}}}{\Delta y}\mathcal{G}^{\mathrm{IV}}_{j,k-\frac{1}{2}} - \frac{\Delta t^{\rho}_{j+\frac{1}{2},k}}{\Delta x}\mathcal{F}^{\mathrm{IV}}_{j+\frac{1}{2},k}\\ &\ge \bar{\rho}_{j,k}(t) + \frac{\Delta x\,\bar{\rho}_{j,k}(t)}{\mathcal{F}^{\mathrm{IV}}_{j+\frac{1}{2},k}\Delta y - \mathcal{G}^{\mathrm{IV}}_{j,k-\frac{1}{2}}\Delta x}\mathcal{G}^{\mathrm{IV}}_{j,k-\frac{1}{2}}\\ &\quad - \frac{\Delta y\,\bar{\rho}_{j,k}(t)}{\mathcal{F}^{\mathrm{IV}}_{j+\frac{1}{2},k}\Delta y - \mathcal{G}^{\mathrm{IV}}_{j,k-\frac{1}{2}}\Delta x}\mathcal{F}^{\mathrm{IV}}_{j+\frac{1}{2},k} = 0,\end{aligned}$$

which shows that $\bar{\rho}_{j,k}(t+\Delta t) \ge 0$ for all j, k, provided that $\bar{\rho}_{j,k}(\Delta t) \ge 0$ for all j, k.

The positivity proof for the c component of the solution can be obtained similarly, and the proof of the theorem will be completed. □

Remark 2 We would like to emphasize that unlike Theorem 1, Theorem 3 guarantees positivity of ρ and c independently of the CFL condition. However, taking large Δt will affect the stability of the fourth-order scheme. In practice, we have used the same CFL condition (2.13) when implemented the fourth-order method.

Remark 3 Note that the positivity-preserving property of the second-order scheme can be also enforced using the "draining" time step technique instead of the adaptive reconstruction approach implemented in Section 2.1.

Parabolic-Elliptic Case ($\alpha = 0$) In this case, the scheme (2.26) is a system of DAEs. The second equation in (2.26) is a system of linear algebraic equations for $c_{j,k}$, which, as before, is to be solved by an accurate and efficient linear algebra solver. However, the matrix of this linear system is no longer diagonally dominant, and thus the positivity of c is not guaranteed (the positivity of ρ is enforced the same way as in the parabolic-parabolic case). At the same time, in our numerical experiments, we have never observed any negative values of c. We would also like to stress that even if some small negative values of c appear, this would not lead to any negative blowup similar to the ones observed in [9, Example 1], where appearance of small negative values of ρ led the computed cell density to a meaningless negative blowup.

3 Numerical experiments

In this section, we test the developed second- and fourth-order hybrid FVFD schemes on two numerical examples. In all of the examples, we have employed the zero Neumann boundary conditions implemented using the standard ghost cell/ghost point technique. The second-order scheme is implemented using the three-state third-order SSP RK method, while the fourth-order scheme is realized using the five-stage fourth-order SSP RK method. In both cases, time steps were chosen to ensure the positivity of the computed densities and changed adaptively according to the CFL

conditions identified in Theorems 1 and 2 for the second-order scheme and in Theorem 3 for the fourth-order scheme.

3.0.1 Example 1—fast blowup in the PKS chemotaxis model

In the first example taken from [9], we consider the initial-boundary value problem (IBVP) for the PKS system (1.1) with $\chi = \gamma_c = \gamma_\rho = \alpha = 1$ in a square domain $[-\frac{1}{2}, \frac{1}{2}] \times [-\frac{1}{2}, \frac{1}{2}]$ subject to the radially symmetric bell-shaped initial data:

$$\rho(x, y, 0) = 1000\, e^{-100(x^2+y^2)}, \quad c(x, y, 0) = 500\, e^{-50(x^2+y^2)}. \tag{3.1}$$

As it was demonstrated in [9], the solution of this IBVP is expected to develop a δ-type singularity at the center of the computational domain in a very short time.

We first implement the proposed second- and fourth-order hybrid FVFD schemes on a uniform mesh with $\Delta x = \Delta y = 1/201$. The cell densities computed at two pre-blowup times $t = 10^{-6}$ and 5×10^{-6}, at which the solution still preserves its initial shape, are shown in Fig. 1. We also compute the solution at near-blowup $t = 7.5 \times 10^{-5}$ and past-blowup $t = 1.5 \times 10^{-4}$ times, and plot the obtained cell densities in Fig. 2. As one can see, the obtained solutions are oscillation-free and the spiky structure is quite accurately resolved by both schemes, but the blowup phenomenon is better resolved by the fourth-order method.

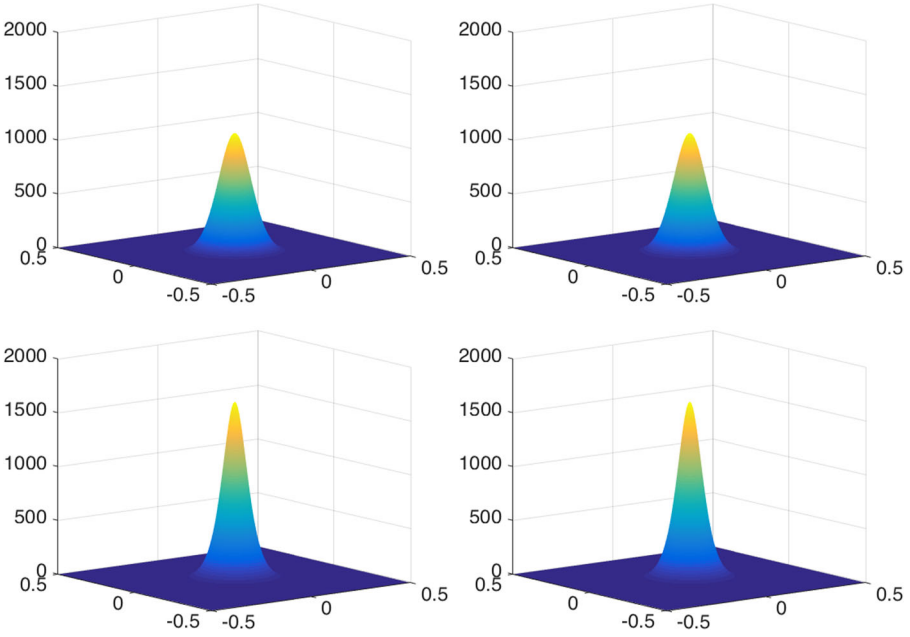

Fig. 1 Example 1: ρ computed by the proposed second- (*left column*) and fourth-order (*right column*) schemes on a uniform mesh with $\Delta x = \Delta y = 1/201$ at pre-blowup times $t = 10^{-6}$ (*top row*) and 5×10^{-6} (*bottom row*)

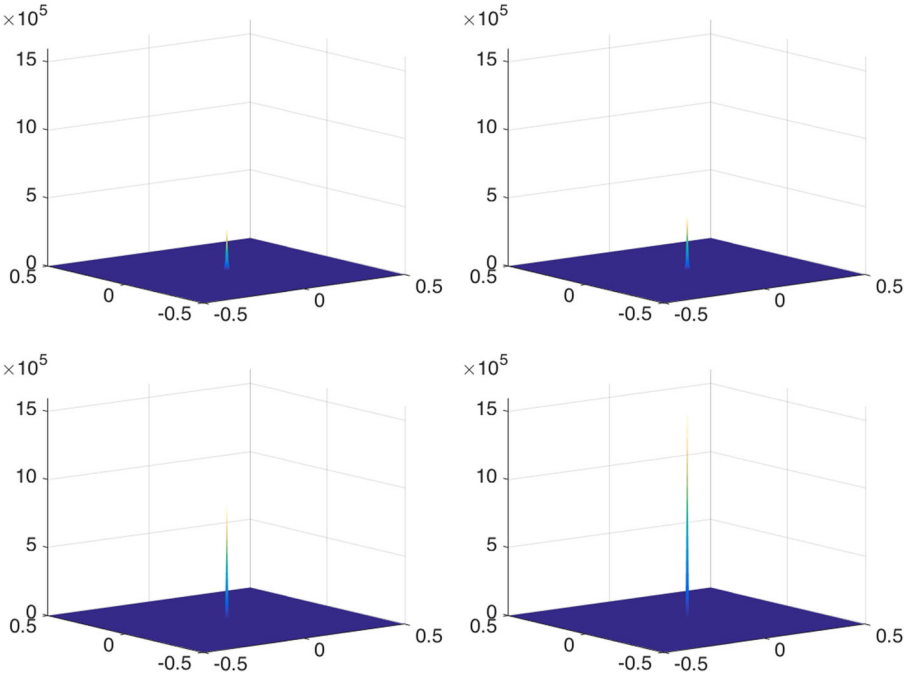

Fig. 2 Example 1: The same as in Fig. 1, but at near-blowup 7.5×10^{-5} (*top*) and past-blowup 1.5×10^{-4} (*bottom*) times

Next, we conduct a comparison study of the second- and fourth-order schemes. We first perform the accuracy test at a small pre-blowup time $t = 10^{-6}$, at which the solution of the IBVP (1.1), (3.1) is smooth. In order to measure the convergence rate, we compute the solutions on a five different grids and compare the obtained results with the reference solution, computed by the proposed fourth-order method on a fine mesh with $\Delta x = \Delta y = 1/801$. The results are presented in Tables 1 and 2, where one can clearly observe an expected or even higher order of convergence for both ρ and c.

Finally, we numerically investigate the blowup in the PKS system by plotting the time evolution of $||\rho||_\infty$ computed by both the second- and fourth-order schemes on three consecutive meshes; see Fig. 3. The vertical lines in these figures indicate the

Table 1 Example 1: L^∞-errors for ρ and c and experimental rates of convergence for the second-order scheme

Grid	ρ-error	Rate	c-error	Rate
101 × 101	2.88E–1		2.44E–4	
201 × 201	6.90E–2	2.09	6.18E–5	2.00
301 × 301	3.04E–2	2.03	2.76E–5	2.00
401 × 401	1.71E–2	2.01	1.55E–5	2.00
501 × 501	1.09E–2	2.01	9.95E–6	2.00

Table 2 Example 1: L^∞-errors for ρ and c and experimental rates of convergence for the fourth-order scheme

Grid	ρ-error	Rate	c-error	Rate
101×101	7.56E-4		1.59E-6	
201×201	1.26E-5	5.94	1.01E-7	4.00
301×301	1.15E-6	5.95	1.99E-8	4.04
401×401	2.07E-7	5.96	6.03E-9	4.16
501×501	5.34E-8	6.09	2.24E-9	4.46

numerical blowup times that are the times by which the value of $||\rho||_\infty$ increases by a factor of four as the grid is refined since the magnitude of finite-volume approximations of a δ-type singularity is always proportional to $1/(\Delta x \Delta y)$. As one can observe, the numerical blowup times for the second- and fourth-order schemes are quite different: the solution computed by the second-order scheme blows up at about $t \approx 1.2 \times 10^{-4}$, while its fourth-order counterpart blows up at an earlier time $t \approx 1.1 \times 10^{-4}$. This together with the fact that the magnitude of the fourth-order solution is about twice larger than the magnitude of the second-order one at the time of blowup, indicate that the use of a higher-order scheme is advantageous when the blowup time should be estimated numerically.

3.0.2 Example 2—slow blowup in the PKS chemotaxis model

In this example also taken from [9], we consider the same IBVP as in Example 1, but with the uniform initial condition for the chemoattractant concentration:

$$c(x, y, 0) = 0.$$

According to [9], the solution of this IBVP develops the same δ-type singularity as in Example 1, but at a much later time.

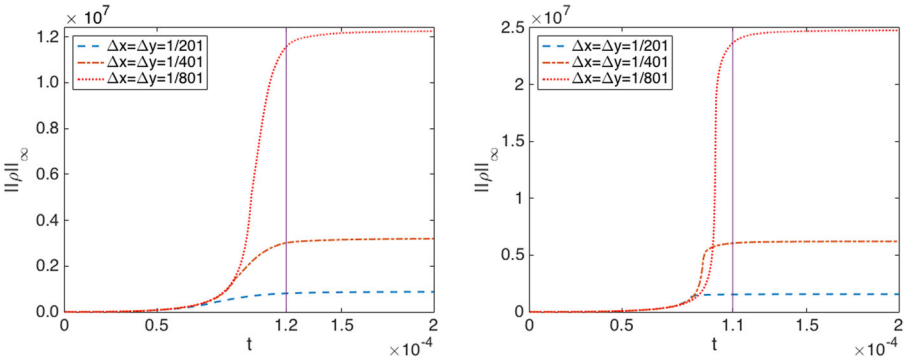

Fig. 3 Example 1: Time evolution of $||\rho||_\infty$ for the second- (*left*) and fourth-order (*right*) schemes on three consecutive meshes. The numerical blowup times are indicated by the corresponding vertical lines

We implement the proposed second- and forth-order hybrid FVFD schemes on a uniform mesh with $\Delta x = \Delta y = 1/201$. The cell densities computed at a pre-blowup time $t = 0.3$ and a past-blowup time $t = 0.4$ are presented in Fig. 4. One can observe that the obtained solutions are oscillation-free, and both of the second- and fourth-order scheme can capture the spiky structure of the solutions. The blowup phenomenon is however better resolved by the fourth-order scheme. This can be seen if the maximum cell density values are compared: while for the second-order results, $\max_x \rho(x, 0.3) \approx 1626.7$, the fourth-order maximum is substantially larger, $\max_x \rho(x, 0.3) \approx 1713.9$.

We also numerically study the blowup phenomenon by plotting the time evolution of $||\rho||_\infty$ computed by both the second- and fourth-order schemes on three consecutive meshes with $\Delta x = \Delta y = 1/101$, $1/201$ and $1/801$; see Fig. 5. The numerical blowup time for both schemes are measured based on the way the magnitude of ρ increases (as it has been explained in Example 1): the second-order solution blows up at $t \approx 0.375$, while the fourth-order solution blows up at an earlier time $t \approx 0.35$. One can also see that the magnitude of the fourth-order solution is about twice larger than the magnitude of the second-order one at the past-blowup time. These two facts confirm the advantage of the higher-order scheme when the blowup time should be estimated numerically.

It would also be instructive to look at the actual time-step size Δt used in the numerical simulations. To this end, we provide Fig. 6, where we plot Δt as a function

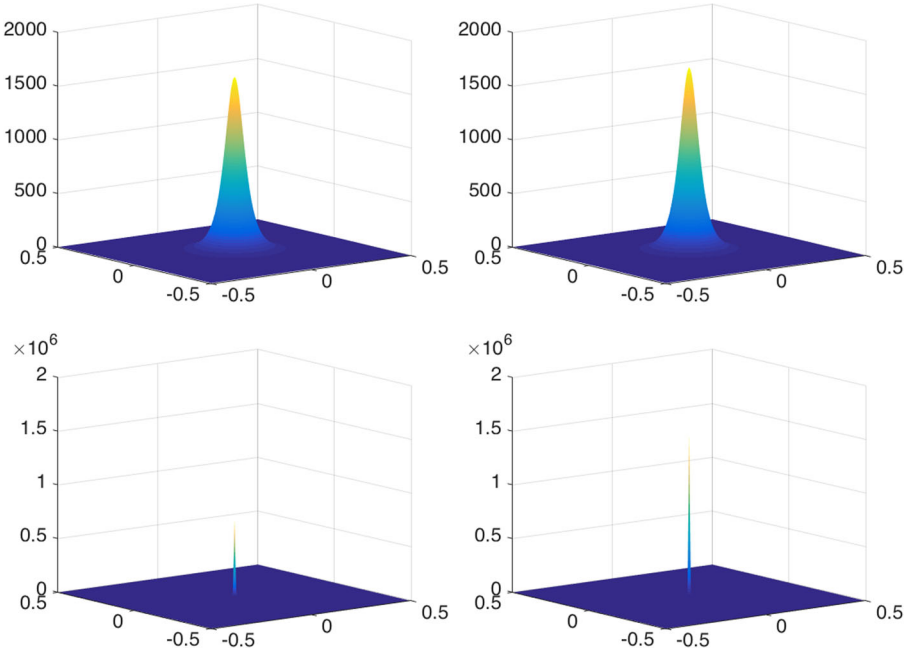

Fig. 4 Example 2: ρ computed by the proposed second- (*left column*) and fourth-order (*right column*) schemes on a uniform mesh with $\Delta x = \Delta y = 1/201$ at pre-blowup $t = 0.3$ (*top row*) and past-blowup $t = 0.4$ (*bottom row*) times

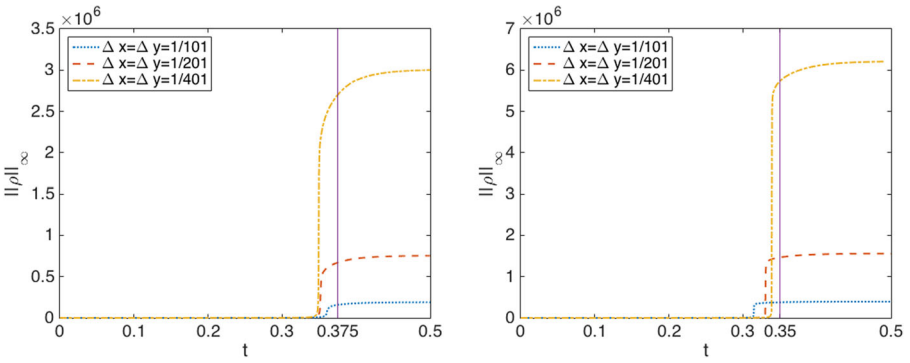

Fig. 5 Example 2: Time evolution of $||\rho||_\infty$ for the second- (*left*) and fourth-order (*right*) schemes on three consecutive meshes. The numerical blowup times are indicated by the corresponding vertical lines

of time t computed by both the second- and fourth-order schemes with $\Delta x = \Delta y = 1/201$. The time-step size is chosen according to the CFL condition specified in (2.13) to guarantee the positivity of the computed solution for both the second- and fourth-order schemes (see Remark 2). As one can see, the upper bound on the time step in (2.13) is a minimum of four terms: The first two, $\Delta x/(8a)$ and $\Delta y/(8b)$, are related to the chemotaxis flux in the first equation in (1.1), while the third and fourth ones are due to the parabolic terms in the system (1.1). In the (near) blowup regime, a and b in (2.13) become large and thus the first two terms determine the size of time steps, in which case an explicit method is efficient enough. However, when a and b are small, the third and fourth terms in (2.13) dominate, which reduces the efficiency of the explicit method. One of the ways to overcome this difficulty is to use positivity preserving implicit-explicit (IMEX) methods [2, 3, 28] as long as a and b remain relatively small; see, e.g., [9]. The implementation of an IMEX algorithm is left outside the scope of the current paper.

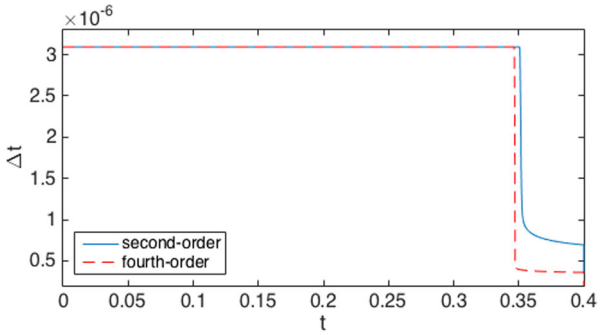

Fig. 6 Example 2: Time step size Δt as a function of time t computed by both the second- and fourth-order schemes with $\Delta x = \Delta y = 1/201$

3.0.3 Example 3—Blowup in the Two-Species Chemotaxis Model

In this example, we consider the IBVP for two-species chemotaxis model

$$\begin{cases} (\rho_1)_t + \nabla\cdot(\chi_1\rho_1\nabla c) = \Delta\rho_1, \\ (\rho_2)_t + \nabla\cdot(\chi_2\rho_2\nabla c) = \Delta\rho_2, \quad (x,y)\in\Omega\subset\mathbb{R}^2, \quad t>0, \\ \Delta c + \rho_1 + \rho_2 - c = 0, \end{cases} \tag{3.2}$$

which was proposed in [49] and then further studied both analytically, [12, 16–20, 34], and numerically, [33]. In (3.2), $\rho_1(x,y,t)$ and $\rho_2(x,y,t)$ denote the cell densities of the first and second non-competing species, $c(x,y,t)$ stands for the chemoattractant concentration, $\chi_2 > \chi_1 > 0$ are the chemotactic sensitivity constants for the first and second species, respectively.

As it was proven in [16, 18], solutions of (3.2) may either remain smooth (with decaying maxima of both ρ_1 and ρ_2) or blow up in a finite time. Moreover, only simultaneous blowup is possible. However, in the blowup regime ρ_1 and ρ_2 may develop different types of singularities depending on the values of χ_1 and χ_2 and on the initial mass of each species:

$$m_1 := \int\limits_\Omega \rho_1(x,y,0)\,dxdy \quad \text{and} \quad m_2 := \int\limits_\Omega \rho_2(x,y,0)\,dxdy.$$

In particular, if

$$\frac{8\pi m_1}{\chi_1} + \frac{8\pi m_2}{\chi_2} - (m_1+m_2)^2 \geq 0 \quad \text{and} \quad m_2 \geq \frac{8\pi}{\chi_2}, \tag{3.3}$$

then ρ_2 is expected to develop much stronger singularity than ρ_1.

We now numerically study a specific example taken from [33], where the system (3.2) with $\chi_1 = 1$ and $\chi_2 = 20$ was considered on the domain $\Omega = [-3,3]\times[-3,3]$ and subject to the bell-shaped initial data:

$$\rho_1(x,y,0) = \rho_2(x,y,0) = 50e^{-100(x^2+y^2)}. \tag{3.4}$$

In this case, the total masses are $m_1 = m_2 \approx \pi/2$ and the condition (3.3) is satisfied.

Although the schemes presented in Section 2 have been derived for the one-species PKS model, they can be straightforwardly extended to the two-species system (3.2) since the equations for ρ_1 and ρ_2 are only coupled through the c-equation. We note that a detailed description of the second-order hybrid FVFD scheme for the two-species model can be found in [33].

We first conduct numerical simulations using both the second- and fourth-order schemes on a uniform mesh with $\Delta x = \Delta y = 6/201$. The cell densities ρ_1 and ρ_2 computed at time $t = 3.3\times10^{-3}$ are presented in Fig. 7. As in Example 1, one can observe that while both schemes accurately capture the spiky structure of the solution, the fourth-order scheme achieves a higher resolution of the blowup phenomenon.

Next, we numerically investigate the blowup behavior of the system (3.2) by plotting the time evolution of $||\rho_1||_\infty$ and $||\rho_2||_\infty$ computed by both second- and fourth-order schemes on the four consecutive uniform meshes with $\Delta x = \Delta y = 6/201, 6/401, 6/801$ and $6/1601$; see Figs. 8 and 9. We measure the numerical

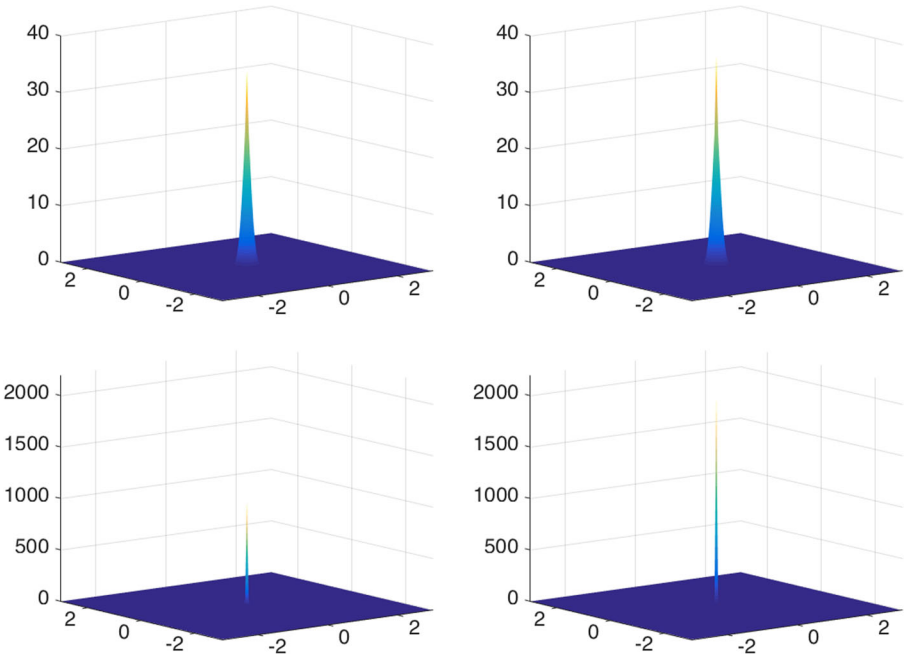

Fig. 7 Example 3: ρ_1 (*top row*) and ρ_2 (*bottom row*) computed by the second- (*left column*) and fourth-order (*right column*) schemes on a uniform mesh with $\Delta x = \Delta y = 6/201$ at time $t = 3.3 \times 10^{-3}$

blowup time for both schemes based on the way the magnitude of ρ_2 increases (as it has been explained in Example 1) and observe that the second-order solution blows up at about $t = 3.8 \times 10^{-3}$, while the fourth-order solution blows up a little earlier at about $t = 3.3 \times 10^{-3}$. However, $||\rho_1||_\infty$ behaves completely different from $||\rho_2||_\infty$: it first decreases, then increases and at the blowup time the maximum of ρ_1 is significantly smaller than the maximum of ρ_2. Looking at the results in Fig. 8, one may conclude that only ρ_2 blows up, but the analytical results proved in [16, 18] state that

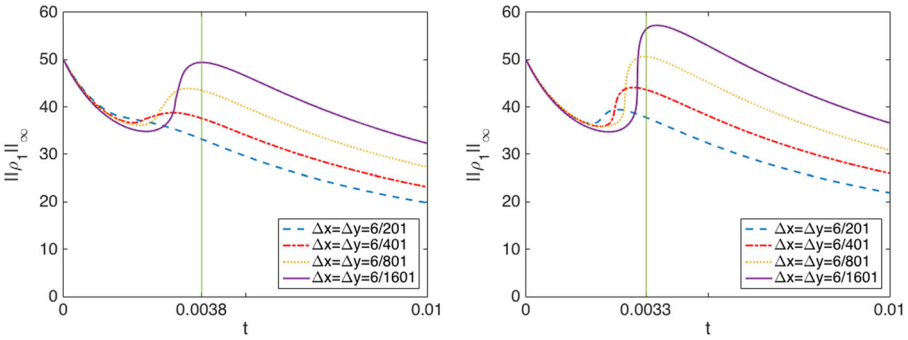

Fig. 8 Example 3: $||\rho_1||_\infty$ as a function of t computed by the second- (*left*) and fourth-order (*right*) schemes. The numerical blowup times are indicated by the corresponding vertical lines

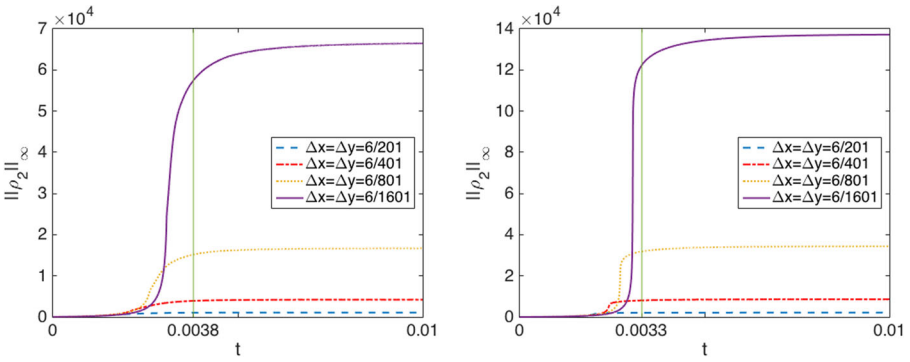

Fig. 9 Example 3: $||\rho_2||_\infty$ as a function of t computed by the second- (*left*) and fourth-order (*right*) schemes. The numerical blowup times are indicated by the corresponding vertical lines

only simultaneous blowup is possible, which suggests that the maximum of ρ_1 should also blow up at about $t = 3.3 \times 10^{-3}$ though at a much slower rate than the maximum of ρ_2. In order to numerically verify this, we perform a mesh refinement study and monitor $||\rho_1||_\infty$ and $||\rho_2||_\infty$ as functions of Δx, which is equal to Δy in this numerical experiment. These functions are presented in Fig. 10. As one can see from Fig. 10 (left), the maximum of ρ_1 computed by the second-order scheme behaves like the function $f_1^{II}(\Delta x) = 9(\frac{3.51}{\Delta x} + 90)^{1/4}$, while the maximum of ρ_1 computed by the fourth-order scheme behaves like the function $f_1^{IV}(\Delta x) = 11.15(\frac{2.94}{\Delta x} + 25)^{1/4}$. This shows that ρ_1 blows up at the rate of

$$||\rho_1||_\infty \sim \frac{1}{(\Delta x \Delta y)^{\frac{1}{8}}}.$$

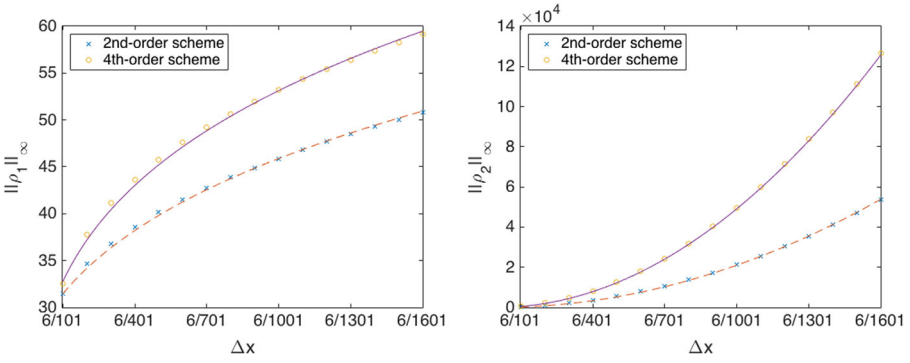

Fig. 10 Example 3: $||\rho_1(x, y, 0.0033)||_\infty$ computed by the second- and fourth-order schemes plotted along with the functions $f_1^{II}(\Delta x) = 9(\frac{3.51}{\Delta x} + 90)^{1/4}$ and $f_1^{IV}(\Delta x) = 11.15(\frac{2.94}{\Delta x} + 25)^{1/4}$ (*left*) and $||\rho_2(x, y, 0.0033)||_\infty$ computed by the second- and fourth-order schemes plotted along with the functions $f_2^{II}(\Delta x) = \frac{0.756}{(\Delta x)^2}$ and $f_2^{IV}(\Delta x) = \frac{1.656}{(\Delta x)^2}$ (*right*) for $\Delta x = \Delta y = 6/101, 6/201, \ldots, 6/1601$

At the same time, Fig. 10 (right) illustrates that $||\rho_2||_\infty$ behaves like $f_2^{II}(\Delta x) = \frac{0.756}{(\Delta x)^2}$ for the second-order results and like $f_2^{IV}(\Delta x) = \frac{1.656}{(\Delta x)^2}$ for the fourth-order ones. This indicates that ρ_2 collapses to a δ-type singularity as

$$||\rho_2||_\infty \sim \frac{1}{\Delta x \Delta y}.$$

We would like to emphasize that even though both the second- and fourth-order schemes asymptotically behave in a similar way in the blowup regime, the magnitude of both ρ_1 and ρ_2 are substantially larger in the fourth-order computations; see Figs. 8–10. This clearly demonstrates the main advantage of using higher-order methods for the two-species chemotaxis system. At the same time, it seems to be necessary to use either adaptive mesh refinement or adaptive moving mesh technique to numerically detect the blowup in ρ_1 in a more convincing way. Development of adaptive techniques for the chemotaxis systems is beyond the scope of this paper and is left for future studies.

Acknowledgments The work of A. Chertock was supported in part by NSF grant DMS-1521051. The work of A. Kurganov was supported in part by NSF grant DMS-1521009.

References

1. Adler, A.: Chemotaxis in bacteria. Ann. Rev. Biochem. **44**, 341–356 (1975)
2. Ascher, U.M., Ruuth, S.J., Spiteri, R.J.: Implicit-explicit runge-kutta methods for time-dependent partial differential equations. Appl. Numer. Math. **25**(2-3), 151–167 (1997)
3. Ascher, U.M., Ruuth, S.J., Wetton, B.T.: Implicit-explicit methods for time-dependent partial differential equations. SIAM J. Numer. Anal. **32**(3), 797–823 (1995)
4. Bollermann, A., Noelle, S., Lukáčová-medviďová, M.: Finite volume evolution Galerkin methods for the shallow water equations with dry beds. Commun. Comput. Phys. **10**(2), 371–404 (2011)
5. Bonner, J.T.: The Cellular Slime Molds, 2nd edn. Princeton University Press, Princeton, New Jersey (1967)
6. Budrene, E.O., Berg, H.C.: Complex patterns formed by motile cells of escherichia coli. Nature **349**, 630–633 (1991)
7. Budrene, E.O., Berg, H.C.: Dynamics of formation of symmetrical patterns by chemotactic bacteria. Nature **376**, 49–53 (1995)
8. Calvez, V., Carrillo, J.A.: Volume effects in the Keller-Segel model: energy estimates preventing blow-up. J. Math. Pures Appl. (9) **86**(2), 155–175 (2006)
9. Chertock, A., Kurganov, A.: A positivity preserving central-upwind scheme for chemotaxis and haptotaxis models. Numer. Math. **111**, 169–205 (2008)
10. Childress, S., Percus, J.K.: Nonlinear aspects of chemotaxis. Math. Biosc. **56**, 217–237 (1981)
11. Cohen, M.H., Robertson, A.: Wave propagation in the early stages of aggregation of cellular slime molds. J. Theor. Biol. **31**, 101–118 (1971)
12. Conca, C., Espejo, E., Vilches, K.: Remarks on the blowup and global existence for a two species chemotactic Keller-Segel system in $\mathbb{R}^2$. European J. Appl. Math. **22**(6), 553–580 (2011)
13. Epshteyn, Y.: Upwind-difference potentials method for Patlak-Keller-Segel chemotaxis model. J. Sci. Comput. **53**(3), 689–713 (2012)
14. Epshteyn, Y., Izmirlioglu, A.: Fully discrete analysis of a discontinuous finite element method for the Keller-Segel chemotaxis model. J. Sci. Comput. **40**(1-3), 211–256 (2009)
15. Epshteyn, Y., Kurganov, A.: New interior penalty discontinuous galerkin methods for the Keller-Segel chemotaxis model. SIAM J. Numer. Anal. **47**, 386–408 (2008)
16. Espejo, E.E., Stevens, A., Suzuki, T.: Simultaneous blowup and mass separation during collapse in an interacting system of chemotactic species. Differential Integral Equations **25**(3-4), 251–288 (2012)

17. Espejo, E.E., Stevens, A., Velázquez, J.J.L.: A note on non-simultaneous blow-up for a drift-diffusion model. Differential Integral Equations **23**(5-6), 451–462 (2010)
18. Espejo, E.E., Vilches, K., Conca, C.: Sharp condition for blow-up and global existence in a two species chemotactic Keller-Segel system in $\mathbb{R}^2$. European J. Appl. Math. **24**, 297–313 (2013)
19. Espejo Arenas, E.E., Stevens, A., Velázquez, J.J.L.: Simultaneous finite time blow-up in a two-species model for chemotaxis. Analysis (Munich) **29**(3), 317–338 (2009)
20. Fasano, A., Mancini, A., Primicerio, M.: Equilibrium of two populations subject to chemotaxis. Math. Models Methods Appl. Sci. **14**, 503–533 (2004)
21. Filbet, F.: A finite volume scheme for the patlak-keller-segel chemotaxis model. Numer. Math. **104**, 457–488 (2006)
22. Gottlieb, S., Ketcheson, D., Shu, C.W.: Strong stability preserving Runge-Kutta and multistep time discretizations. World Scientific Publishing Co. Pte. Ltd., Hackensack NJ (2011)
23. Gottlieb, S., Shu, C.W., Tadmor, E.: Strong stability-preserving high-order time discretization methods. SIAM Rev. **43**, 89–112 (2001)
24. Herrero, M.A., Velázquez, J.J.L.: A blow-up mechanism for a chemotaxis model. Ann. Sc. Norm. Super. **24**, 633–683 (1997)
25. Hillen, T., Painter, K.J.: A user's guide to PDE models for chemotaxis. J. Math. Biol. **58**(1-2), 183–217 (2009)
26. Horstmann, D.: From 1970 until now: The keller-segel model in chemotaxis and its consequences i. Jahresber. DMV **105**, 103–165 (2003)
27. Horstmann, D.: From 1970 until now: The keller-segel model in chemotaxis and its consequences ii. Jahresber. DMV **106**, 51–69 (2004)
28. Hundsdorfer, W., Verwer, J.G.: Numerical solution of time-dependent advection-diffusion-reaction equations, vol. 33 Springer Science & Business Media (2013)
29. Keller, E.F., Segel, L.A.: Initiation of slime mold aggregation viewed as an instability. J. Theor. Biol. **26**, 399–415 (1970)
30. Keller, E.F., Segel, L.A.: Model for chemotaxis. J. Theor. Biol. **30**, 225–234 (1971)
31. Keller, E.F., Segel, L.A.: Traveling bands of chemotactic bacteria: a theoretical analysis. J. Theor. Biol. **30**, 235–248 (1971)
32. Kurganov, A., Liu, Y.: New adaptive artificial viscosity method for hyperbolic systems of conservation laws. J. Comput. Phys. **231**, 8114–8132 (2012)
33. Kurganov, A., Lukáčová-medviďová, M.: Numerical study of two-species chemotaxis models. Discrete Contin. Dyn. Syst. Ser. B **19**, 131–152 (2014)
34. Kurokiba, M., Ogawa, T.: Finite time blow-up of the solution for a nonlinear parabolic equation of drift-diffusion type. Diff. Integral Eqns **4**, 427–452 (2003)
35. van Leer, B.: Towards the ultimate conservative difference scheme. V. A second-order sequel to Godunov's method. J. Comput. Phys. **32**(1), 101–136 (1979)
36. Lie, K.A., Noelle, S.: On the artificial compression method for second-order nonoscillatory central difference schemes for systems of conservation laws. SIAM J. Sci. Comput. **24**(4), 1157–1174 (2003)
37. Marrocco, A.: 2d simulation of chemotaxis bacteria aggregation. m2AN. Math. Model. Numer. Anal. **37**, 617–630 (2003)
38. Nanjundiah, V.: Chemotaxis, signal relaying and aggregation morphology. J. Theor. Biol. **42**, 63–105 (1973)
39. Nessyahu, H., Tadmor, E.: Nonoscillatory central differencing for hyperbolic conservation laws. J. Comput. Phys. **87**(2), 408–463 (1990)
40. Patlak, C.S.: Random walk with persistence and external bias. Bull. Math: Biophys. **15**, 311–338 (1953)
41. Perthame, B.: PDE models for chemotactic movements: parabolic, hyperbolic and kinetic. Appl. Math. **49**, 539–564 (2004)
42. Perthame, B.: Transport Equations in Biology. Frontiers in Mathematics. Basel, Birkhäuser Verlag (2007)
43. Prescott, L.M., Harley, J.P., Klein, D.A.: Microbiology, 3rd edn. Wm. C. Brown Publishers, Chicago, London (1996)
44. Saito, N.: Conservative upwind finite-element method for a simplified Keller-Segel system modelling chemotaxis. IMA J. Numer. Anal. **27**(2), 332–365 (2007)
45. Strehl, R., Sokolov, A., Kuzmin, D., Turek, S.: A flux-corrected finite element method for chemotaxis problems. Computational Methods in Applied Mathematics **10**(2), 219–232 (2010)

46. Sweby, P.K.: High resolution schemes using flux limiters for hyperbolic conservation laws. SIAM J. Numer. Anal. **21**(5), 995–1011 (1984)
47. Tyson, R., Lubkin, S.R., Murray, J.D.: Model and analysis of chemotactic bacterial patterns in a liquid medium. J. Math. Biol. **38**(4), 359–375 (1999)
48. Tyson, R., Stern, L.G., LeVeque, R.J.: Fractional step methods applied to a chemotaxis model. J. Math. Biol. **41**, 455–475 (2000)
49. Wolansky, G.: Multi-components chemotactic system in the absence of conflicts. European J. Appl. Math. **13**, 641–661 (2002)
50. Woodward, D., Tyson, R., Myerscough, M., Murray, J., Budrene, E., Berg, H.: Spatio-temporal patterns generated by S. typhimurium. Biophys. J. **68**, 2181–2189 (1995)